Energy & Environmental Science

Accepted Manuscript

This article can be cited before page numbers have been issued, to do this please use: Y. Peng, B. Akuzum, N. Kurra, M. Zhao, M. Alhabeb, B. Anasori , E. C. Kumbur, H. N. Alshareef, M. D. Ger and Y. Gogotsi, *Energy Environ. Sci.*, 2016, DOI: 10.1039/C6EE01717G.

ROYAL SOCIETY OF CHEMISTRY

www.rsc.org/ees

Energy & Environmental Science

DOI: 10.1039/C6EE01717G

PAPER

All-MXene (2D titanium carbide) Solid-State Microsupercapacitors for On-Chip Energy Storage

Received 00th January 20xx,
Accepted 00th January 20xx

DOI: 10.1039/x0xx00000x

www.rsc.org/

You-Yu Peng[a,b,e], Bilen Akuzum[b,c], Narendra Kurra[b,d], Meng-Qiang Zhao[b], Mohamed Alhabeb[b], Babak Anasori[b], Emin Caglan Kumbur[c], Husam N. Alshareef[d], Ming-Der Ger[e], Yury Gogotsi*[b]

On-chip energy storage is a rapidly evolving research topic, opening doors for integration of batteries and supercapacitors at microscales on rigid and flexible platforms. Recently, a new class of two-dimensional (2D) transition metal carbides and nitrides (so-called MXenes) has shown great promise in electrochemical energy storage applications. Here, we report the farbication of all-MXene ($Ti_3C_2T_x$) solid-state interdigital microsupercapacitors by employing a solution spray-coating, followed by a photoresist-free direct laser cutting method. Our prototype devices consisted of two layes of $Ti_3C_2T_x$ with two different flake sizes. The bottom layer was stacked large-size MXene flakes (lateral dimensions of 3-6 µm) serving mainly as current collectors. The top layer was made of small-size MXene flakes (~1 µm) with a large number of defects and edges as the electroactive layer responsible for energy storage. Compared to $Ti_3C_2T_x$ micro-supercapacitors with platinum current collectors, the all-MXene devices exhibited much lower contact resistance, higher capacitances and better rate-capabilities. The areal and volumetric capacitances of ~27 mF cm^{-2} and ~357 F cm^{-3}, respectively, at a scan rate of 20 mV s^{-1} were achieved. The devices also demonstrated their excellent cyclic stability, with 100 % capacitance retention after 10,000 cycles at a scan rate of 50 mV s^{-1}. This study opens up a plethora of possible designs for high-performance on-chip devices employing different chemistries, flake sizes and morphologies of MXenes and their heterostructures.

Broader context

The continuous development and further miniaturization of portable electronic devices and microelectromechanical systems has led to the increasing demands for micro or nanoscale power sources and energy storage units. Supercapacitors, also called electrochemical capacitors, are energy storage devices with long service life and high power densities that can be fully charged and discharged in seconds. Small-scale supercapacitors, or micro-supercapacitors (MSCs), can be integrated with self-powered microscale devices and provide the required power for a long duration of time without maintenance, serving as ideal stand-alone power sources. The intrinsic properties of electrode materials play a crucially important role in the performance of MSCs. Here, a novel MSC is fabricated by employing a new material, two-dimensional titanium carbide (MXene). The MXene MSCs offer long lifetime and higher areal and volumetric capacities compared to most of the previously reported devices. This work opens up a door for the design of on-chip devices with high energy storage capability by employing a large family (~ 20 members) of 2D MXenes and their heterostructures.

Introduction

The rapid progress in the field of miniaturized portable electronic devices has stimulated an immense interest for developing micro-scale power sources such as thin film batteries and micro-supercapacitors.[1-3] Micro-supercapacitors (MSCs) are capable of powering up microelectronic devices such as portable personal electronics, micro-electromechanical systems (MEMS), microsensors, and nanorobots. MSCs with interdigitated electrode architectures rely on free movement of electrolyte ions and tend to exhibit superior power density and rate capability over their sandwich counterparts, and a longer cycle life when compared to micro-batteries.[4-6] Thus, interdigitated MSC seems to be a better design option for micro-scale power sources in comparison to the conventional sandwich configuration, as the latter may have issues with ion diffusion across the separator/membrane.[1, 6-8]

Most of the MSCs were fabricated by employing traditional micro-fabrication techniques starting with patterning of the current collectors as the bottom layer, followed by deposition of electro-active materials using techniques such as sputtering, electrophoretic deposition, electrochemical deposition, etc.[1] The intrinsic properties of electrode materials are crucially important for the performance of MSCs. In most cases, carbonaceous materials that store charge through electrical double layer, such as activated carbon,[9] onion-like carbon,[10] carbon nanotubes,[11, 12] carbide-derived carbon,[5, 7] graphene or graphene oxide,[8, 13-17] and their composites,[18, 19] were explored in MSCs. In addition, pseudocapacitive materials involving surface redox reactions, such as transition metal oxides/hydroxides,[20, 21] sulphides (MoS_2,[22] $CoNi_2S_4$,[23] VS_2[24]), and

[a] School of Defense Science, Chung Cheng Institute of Technology, National Defense University, Taoyuan City, Taiwan
[b] A. J. Drexel Nanomaterials Institute, Department of Materials Science and Engineering, Drexel University, Philadelphia, PA 19104, USA
[c] Electrochemical Energy Systems Laboratory, Department of Mechanical Engineering and Mechanics, Drexel University, Philadelphia, PA 19104 USA
[d] Department of Materials Science and Engineering, King Abdullah University of Science and Technology (KAUST), Thuwal, Kingdom of Saudi Arabia
[e] Department of Chemical &Materials Engineering, Chung Cheng Institute of Technology, National Defense University, Taoyuan City, Taiwan
* Corresponding author. E-mail: gogotsi@drexel.edu
Electronic Supplementary Information (ESI) available: See
DOI: 10.1039/x0xx00000x

even conductive polymers,[25, 26] have been used to fabricate high-capacity MSCs. However, the areal and volumetric capacitances, which are two important performance metrics for MSCs, achieved in these MSCs are always limited either due to the low packing density or the poor electrical conductivity of the electrode materials.[1] The high packing density of MoS_2 rendered it as a promising electrode material for energy storage devices with high volumetric energy and power densities.[27] Besides, a new class of two-dimensional (2D) transition metal carbides, carbonitrides and nitrides called MXenes were discovered recently.[28-30] They are synthesized by etching the 'A' layers from their ternary carbides precursors, the MAX phases.[31-34] MXenes have a formula $M_{n+1}X_nT_x$, where M is an early transition metal, X is carbon or nitrogen, n = 1 to 3, and T_x refers to surface functionalities, such as OH, O, and F. They have already shown great promise as potential electrode materials for various energy storage devices, inclding supercapacitors,[35-39] sodium-ion capacitors,[40, 41] lithium-ion,[42, 43] and lithium-sulfur batteries.[44] In general, MXenes' rich chemistry and tuneable surface termination, metallic conductivity, surface hydrophilicity, and high packing densities make them attractive candidates for practical, especially high volumetric energy storage applications.[45]

MXenes could be potential candidate materials for high-performance MSCs due to the following merits: 1) MXenes show high gravimetric capacitances comparable to graphene, while have a much larger packing density (~4.0 g cm^{-3}),[29, 36, 45] which helps to improve the volumetric characteristics. For instance, stable specific volumetric capacitance close to 1000 F cm^{-3} was reported for $Ti_3C_2T_x$ MXenes in a conventional 3-electrode configuration,[36] exceeding all of the carbon-based supercapacitors[46-48]. 2) Most MXenes are metallic conductors with an electrical conductivity up to 6500 S cm^{-1},[49] this enables the fast transfer of electrons and eliminates the need for noble metal current collectors. However, rare study on MXene microsupercapacitors has been reported, in spite the fact that for aligned 2D layers, ion transport is much facile for interdigital architectures compared to stacked electrodes.[50] The only report from Shen et al. demonstrated the fabrication of MXene-based MSC through a filtration and subsequent oxidative etching method. However, a quite low volumetric capacitance of 14.4 F cm^{-3} was obtained. [50]

Herein, we propose a simple yet elegant solution processing approach to fabricate all-MXene-based solid state MSCs. In contrast to most of MSCs reported in the literature, which usually rely on noble metal (gold, platinum, or other alloy) layers as current collectors, we use $Ti_3C_2T_x$ MXenes both as the current collector and active materials. The all-MXene solid-state MSCs exhibited excellent areal and volumetric capacitances and offered great cyclic performance benefited from their homogeneous structures and the excellent electrochemical properties of $Ti_3C_2T_x$ MXene.

Results and discussion

The steps for the fabrication of the on-chip, all-MXene solid-state MSCs is shown in Fig. 1. We employed a spray-coating method to deposit highly conductive large-size $Ti_3C_2T_x$ (L-$Ti_3C_2T_x$) flakes on a glass substrate as the current collector at the bottom (Fig. 1a). It was followed by spray-coating of small-size $Ti_3C_2T_x$ flakes (s-$Ti_3C_2T_x$) on top as an electroactive layer (Fig. 1b). The interdigital pattern was carved by direct laser cutting of a specific centre area of 8 × 6 mm^2 on the stacked MXene film (Fig. 1c). A PVA/H_2SO_4 gel electrolyte was carefully dropped onto the interdigital pattern area and left in air overnight at room temperature to evaporate excess water (Fig. 1d). The final outcome resulted in the "*all-MXene-based solid-state MSCs (L-s-$Ti_3C_2T_x$)*". For the sake of comparison, we also prepared all s-$Ti_3C_2T_x$, all L-$Ti_3C_2T_x$, and Pt/s-$Ti_3C_2T_x$ MSCs with a Pt layer as the current collector, as shown in Fig. S1 in Electronic Supplementary Information (ESI).

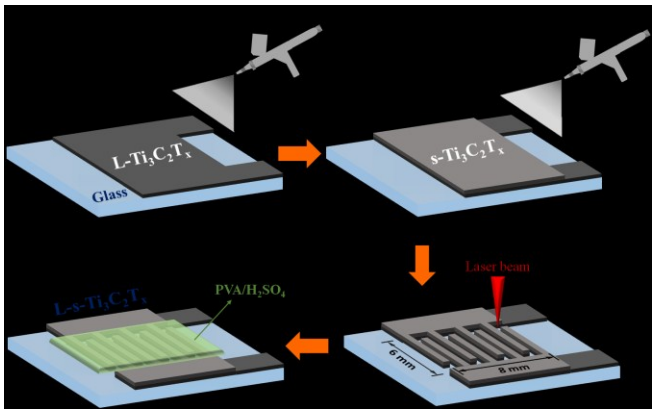

Fig. 1 Schematic illustrating the fabrication process of the all-$Ti_3C_2T_x$ MXene MSC. (a) Spray-coating of a thin L-$Ti_3C_2T_x$ layer at the bottom as the current collector, (b) followed by coating of an electroactive s-$Ti_3C_2T_x$ film. (c) Laser cutting of the L-s-$Ti_3C_2T_x$ film to obtain interdigital electrodes with an area of 8 x 6 mm^2. (d) Painting of a PVA/H_2SO_4 gel electrolyte on the interdigital electrodes to fabricate the MSC device.

Typical transmission electron microscope (TEM) micrographs for individual $Ti_3C_2T_x$ MXene flakes with diverse lateral sizes are shown in Fig. 2a and b. The L-$Ti_3C_2T_x$ flakes are flat and transparent under TEM (Fig. 2a). In contrast, the s-$Ti_3C_2T_x$ flakes (Fig. 2b) are relatively smaller and contain more defects. The lateral size distribution of L-$Ti_3C_2T_x$ is concentrated in the range of 3-6 µm (Fig. 2c), but majority of the s-$Ti_3C_2T_x$ flakes are smaller than 1 µm (Fig. 1d). The differences in lateral dimensions and number of defects of these two MXenes could be governed by their delamination process. The L-$Ti_3C_2T_x$ flakes were obtained by a mild delamination (5-min hand shaking) of the as-etched multi-layer $Ti_3C_2T_x$ particles. The s-$Ti_3C_2T_x$ flakes were prepared by 30-min probe sonication of an L-$Ti_3C_2T_x$ solution, which has fragmented the large flakes into smaller ones and resulted in more structural defects.

The overall crystallinity of these two types of $Ti_3C_2T_x$ MXenes was investigated *via* x-ray diffraction (XRD), as shown in Fig. 2e. Similar to the previously reported $Ti_3C_2T_x$ MXenes,[38] the (002) peaks for both of the two MXenes are located at ~ 7 °, which is due to the intercalation of single layer of water molecules between MXene flakes. Also, there is a small peak at lower 2θ (~6 °), which possibly is due to the presence of two layers of

water molecules between some flakes.[33, 35] Water intercalation into MXenes is common and has been previously observed in other MXenes such as Nb_2CT_x, V_2CT_x, Mo_2CT_x and $Nb_4C_3T_x$.[51-53] Moreover, the (002) peak of s-$Ti_3C_2T_x$ is broader than that of L-$Ti_3C_2T_x$. The full width at half maximums (FWHMs) of s-$Ti_3C_2T_x$ and L-$Ti_3C_2T_x$ were 0.45° and 0.31°, respectively, which can be attributed to the higher degree of MXene layers alignment along the c-axis for the latter. The electrical conductivity of these two MXene films with similar thicknesses was estimated by measuring the generated currents upon applying small bias voltages, as shown in Fig. 2f. It was observed that the L-$Ti_3C_2T_x$ film has lower resistance compared to the s-$Ti_3C_2T_x$ film. Electrical conductivity values of L-$Ti_3C_2T_x$ and s-$Ti_3C_2T_x$ films were measured by a four-point probe as 2508 and 778 S cm^{-1}, respectively. This could be attributed to two effects: (1) The L-$Ti_3C_2T_x$ film had less flake-to-flake contact resistance compared to s-$Ti_3C_2T_x$ due to their large MXene flake size; (2) The s-$Ti_3C_2T_x$ flakes were more defective causing more electrical resistivity. Moreover, having more defects makes s-$Ti_3C_2T_x$ more prone to oxidation in air than L-$Ti_3C_2T_x$, resulting in higher overall resistance.[54]

Fig. 3a shows a digital photograph of an as-fabricated L-s-$Ti_3C_2T_x$ MSC device on a glass substrate, with a United States (US) Dime coin alongside for size comparison. The patterned L-s-$Ti_3C_2T_x$ MXene film electrode was imaged using scanning electron microscopy (SEM). Typical width of the MXene finger electrode was measured to be around 600 µm (Fig. 3b). We have optimized the laser cutting conditions to ensure clear isolation of electrode fingers to avoid any electrical short-circuits while maintaining the minimum spacing between the electrode fingers, as shown in Fig. S2 (ESI). In general, laser head movement is done through electric motors, and there are always some vibrations during the laser cutting process.

In addition, the local heat generated by laser may not be dissipated completely and fast enough through the underneath glass. All these facts result in the uneven nature of laser cutting routes. This is especially true at the corners of the pattern where laser dwell time laser is longer (Fig. 3b). A straight and clean channel of ~110 µm wide was obtained after the optimization (Fig. 3c). The cross-sectional SEM image of the L-s-$Ti_3C_2T_x$ film clearly shows the restacking of the MXene flakes with good alignment after the spray-coating process (Fig. 3d). Thickness of the L-s-$Ti_3C_2T_x$ film was measured by a profilometer (Fig. 3e), and found to be ~1.3 µm as shown in Fig. 3f, which is consistent with the cross-sectional SEM image (as shown in Fig. 3d).

Electrochemical performance of the L-s-$Ti_3C_2T_x$ MSCs was investigated in a two-electrode configuration using PVA/H_2SO_4 gel electrolyte. MXene-based MSCs with other configurations, including Pt/s-$Ti_3C_2T_x$, all L-$Ti_3C_2T_x$, and all s-$Ti_3C_2T_x$ MSCs, were also tested for comparison. Cyclic voltammograms (CVs) of the four kinds of MXene-based MSCs at a scan rate of 50 mV s^{-1} were shown in Fig. 4a. Typical rectangle-like CV curves were obtained for all of them. The CV curves of all these MSC devices at different scan rates were are shown in Fig. S3, ESI. In general, the s-$Ti_3C_2T_x$ MSC has higher areal capacitance when compared to the L-$Ti_3C_2T_x$ MSC. This could be attributed to the small flake size and high concentration of defects of s-$Ti_3C_2T_x$ flakes, leading to more electroactive sites that helped increase the capacitance.[55] In contrast, the L-$Ti_3C_2T_x$ MSC shows better rate-capabilities and faster responsive time compared to the s-$Ti_3C_2T_x$ MSC, possibly due to the superior electrical conductivity of the former. Similar results were obtained by the galvanostatic charge-discharge testing, as shown in Fig. S4, ESI. A typical isosceles triangle shape for the L-$Ti_3C_2T_x$ MSC and obviously IR drop for the s-$Ti_3C_2T_x$ MSC were obtained, respectively, at various current density. At the same current density of 1.0 mA cm^{-2}, a longer discharge time with a serious IR drop for the s-$Ti_3C_2T_x$ MSC was observed compared to the L-$Ti_3C_2T_x$ one (Fig. 4b).

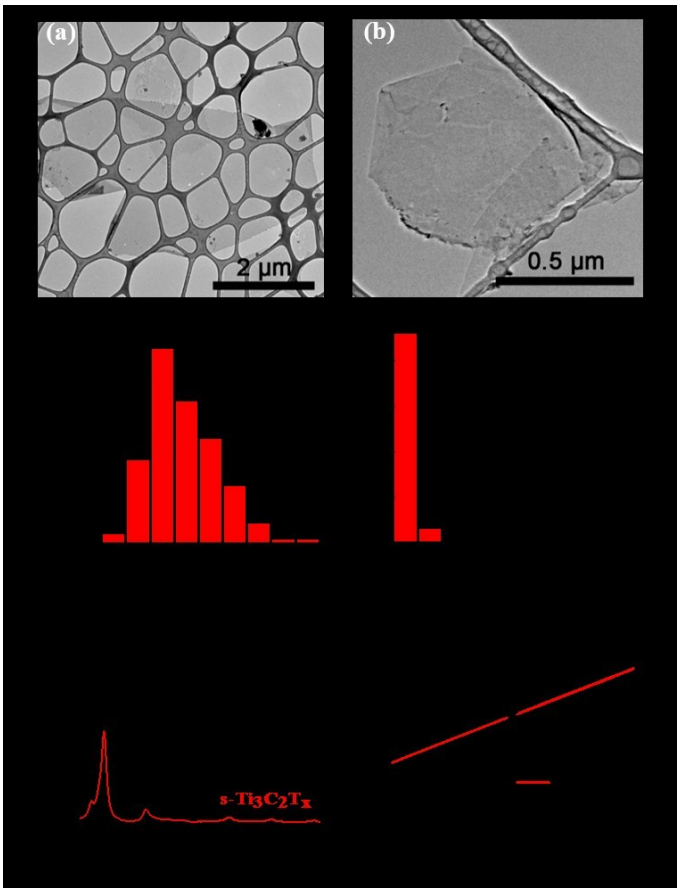

Fig. 2 TEM micrographs showing individual (a) L-$Ti_3C_2T_x$, and (b) s-$Ti_3C_2T_x$ flakes. Flake size distribution of (c) L-$Ti_3C_2T_x$, and (d) s-$Ti_3C_2T_x$. (e) XRD patterns and (f) I-V curves of L-$Ti_3C_2T_x$, and s-$Ti_3C_2T_x$ MXene films.

Energy & Environmental Science

View Article Online
DOI: 10.1039/C6EE01717G

PAPER

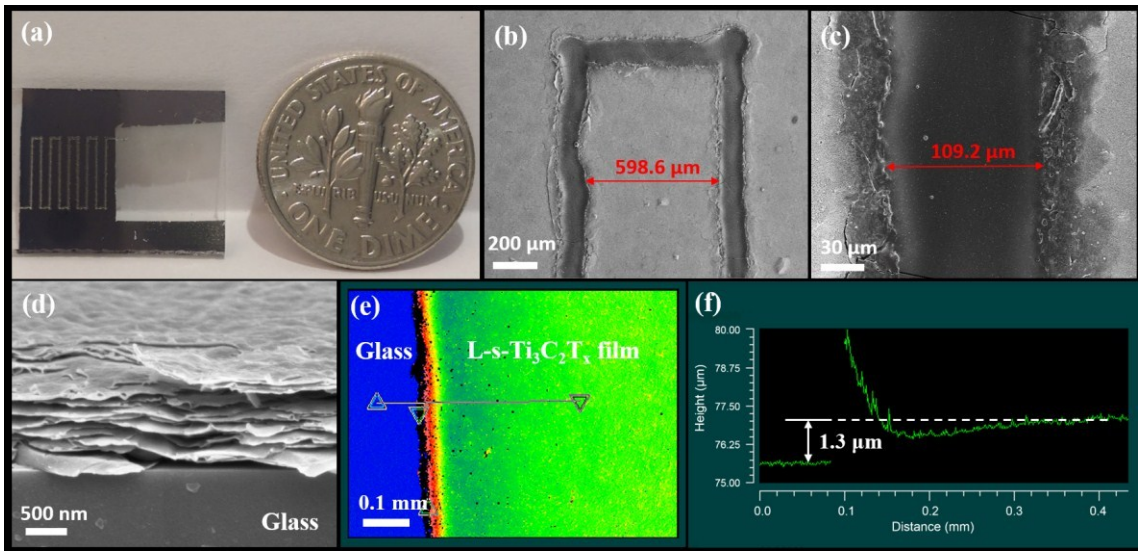

Fig. 3 (a) Digital photograph showing an as-fabricated interdigital L-s-$Ti_3C_2T_x$ MSC on a glass substrate (a Dime coin is shown alongside for size comparison). SEM images showing (b) a laser cut MXene finger electrode (width, ~600 µm) and (c) an interspace region (~110 µm), (d) Cross-sectional SEM image of an entire L-s-$Ti_3C_2T_x$ MXene film on the glass substrate. (e, f) Optical profilometer image used to determine the thickness of an L-s-$Ti_3C_2T_x$ MXene stack film.

The performance of s-$Ti_3C_2T_x$ MSC was improved by using a Pt layer as the current collector and making a Pt/s-$Ti_3C_2T_x$ MSC (Fig. 4a and b). However, by using L-$Ti_3C_2T_x$ instead of Pt as the current collector and making the L-s-$Ti_3C_2T_x$ MSC, not only the highest capacitances and best rectangle shaped CV curves, but also the lowest IR drop were achieved. This benefit came from the combination of the advantages of high capacitance of s-$Ti_3C_2T_x$ and high conductivity of L-$Ti_3C_2T_x$.

Moreover, compared to the devices with a Pt current collector, a uniform interface formed between the current collector (L-$Ti_3C_2T_x$) and the active material (s-$Ti_3C_2T_x$) films in L-s-$Ti_3C_2T_x$ MSC considering their quite similar chemistry. Typical CV curves of the L-s-$Ti_3C_2T_x$ MSC at different scan rates are shown in Fig. 4c, which exhibit good rectangular shape up to 100 mV s^{-1}. Isosceles triangle charge-discharge curves at different current densities are obtained in Fig. 4d, which indicates good Coulombic efficiency of the L-s-$Ti_3C_2T_x$ MSC.

The areal capacitances versus scan rates for the four MXene-based MSC kinds are calculated and shown in Fig. 4e. The significant performance differences between the s-$Ti_3C_2T_x$ and L-$Ti_3C_2T_x$ MSCs are observed again. The s-$Ti_3C_2T_x$ MSC exhibits an areal capacitance of 19.6 mF cm^{-2} at 20 mV s^{-1}, which decreases drastically to 1.0 mF cm^{-2} at 2 V s^{-1}, with only 5% retention. In contrast, the L-$Ti_3C_2T_x$ MSC shows 12.5 mF cm^{-2} of capacitance at 20 mV s^{-1}, but 24% (3.0 mF cm^{-2}) retention at 2 V s^{-1}. Although the capacitance of s-$Ti_3C_2T_x$ is increased from 19.6 to 23.6 mF cm^{-2} by using the Pt current collector in Pt/s-$Ti_3C_2T_x$ MSC, its capacitance retention is only 14%, from 20 to 2000 mV s^{-1}. For the L-s-$Ti_3C_2T_x$ MSC, areal capacitance values as high as 27.3 mF cm^{-2} at a scan rate of 20 mV s^{-1} are observed, with a good 24% capacitance retention at the high scan rate of 2 V s^{-1}. The volumetric capacitances of these four MXene-based MSC devices are also calculated and compared in Fig. S5 (ESI). High volumetric capacitances of 356.8 F cm^{-3} at a current density of 0.2 mA cm^{-2} and 337.5 F cm^{-3} at 20 mV s^{-1} were achieved for the L-s-$Ti_3C_2T_x$ MSC. At 4 mA cm^{-2} and 2 V s^{-1}, these values were retained as ~250 and ~100 F cm^{-3}, respectively.

The areal capacitance of the L-s-$Ti_3C_2T_x$ MSC achieved here is superior to most of carbon-based MSCs such as activated carbon (2.3 mF cm^{-2}),[9] onion-like carbon (1.7 mF cm^{-2}),[10] carbon nanotubes (0.4 mF cm^{-2}),[11] reduced graphene oxide (rGO), graphene, porous graphene, and exfoliated graphene (0.1 – 5.4 mF cm^{-2}),[8, 14-17, 56] graphene/carbon nanotubes composites (2.1 – 6.1 mF cm^{-2}),[18, 57] cobalt hydroxide/reduced graphene oxide ($Co(OH)_2$/rGO) (6 mF cm^{-2}),[25] and comparable to carbon coating of vertically Si nanowire (C@SiNWs) (25.6 mF cm^{-2}).[58]

The electrochemical capacitive behaviour of the four MSCs was further investigated by electrochemical impedance spectroscopy, as shown in Fig. 4f. The different solution resistance between the L-$Ti_3C_2T_x$ and s-$Ti_3C_2T_x$ MSCs at high frequency can be attributed to difference in electrical conductivity of the films. The contact resistances for Pt/s-$Ti_3C_2T_x$ and L-s-$Ti_3C_2T_x$ MSC devices were calculated to be 20.4 and 7.1 $\Omega.cm^2$, respectively. This indicates that the unique combination of L- and s-$Ti_3C_2T_x$ flakes eliminates the large contact resistance between the current collector and active materials, facilitates

Energy & Environmental Science PAPER

the efficient charge transfer across the interface, and in turn, enhances the overall electrochemical performance. The higher 45° slope of the L-$Ti_3C_2T_x$ MSC at middle frequency portion indicated longer ion transport path during the charge-discharge process possibly due to its larger flake sizes. In the case, more ion channels were available in the structure set up by smaller flakes (s-$Ti_3C_2T_x$). By combing the small and large flakes MXenes, the lowest resistance and best capacitive behaviour were obtained for the L-s-$Ti_3C_2T_x$ MSC, indicating a perfect synergy of the s-$Ti_3C_2T_x$ and L-$Ti_3C_2T_x$ flakes.

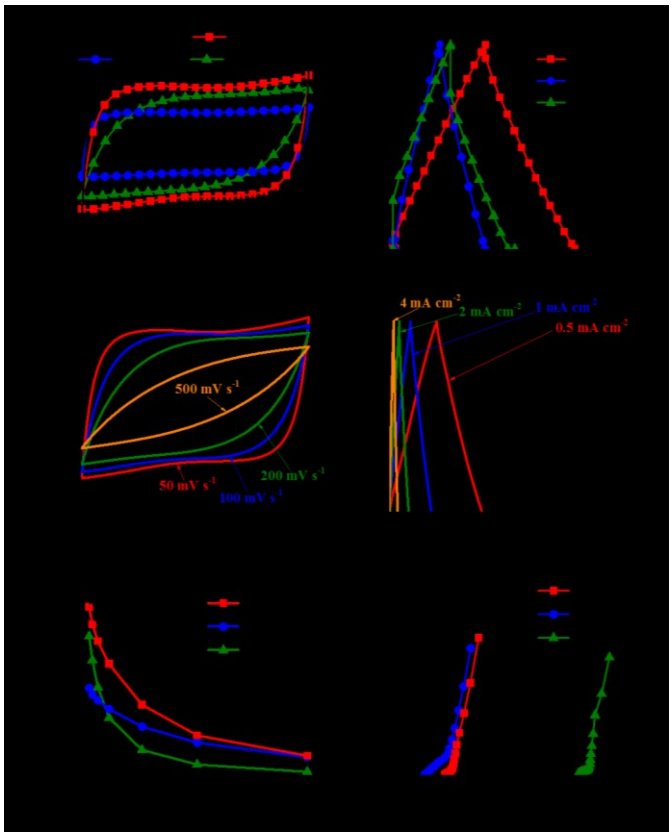

Fig. 4 Electrochemical performance of MXene-based MSC devices. (a) CVs at a scan rate of 50 mV s^{-1} and (b) charge-discharge curves at a current density of 1 mA cm^{-2} of various MSC devices; (c) CV curves of the L-s-$Ti_3C_2T_x$ MSC at different scan rates; (d) Charge-discharge profiles of the L-s-$Ti_3C_2T_x$ MSC at different current densities; (e) Variation in areal capacitances with scan rates and (f) the Nyquist plots for the four MXene-based MSC devices.

Note that the $Ti_3C_2T_x$ MXene can be oxidized in aqueous electrolytes with oxygen and positive potentials,[45] which will result in capacitance decay during the cyclic tests and increase of resistance (Fig. S6a-c, ESI). As a result, a colour change from black to yellow grey occurred for the positive electrode, indicating the transformation of $Ti_3C_2T_x$ to titania after the tests (Fig. S6b, ESI). In order to improve the cycling stability of the all-MXene-based MSCs, we performed a simple sonication-assisted degassing process to remove the trapped oxygen in the electrolyte. After this step, upon 100% capacitance retention was observed for L-s-$Ti_3C_2T_x$ MSC over 10,000 cycles at a scan rate of 50 mV s^{-1} (Fig. S6d, ESI). The fluctuations of the cycling stability can be attributed to the competition of $Ti_3C_2T_x$ oxidation by residual oxygen in the electrolyte (decrease) and the improved electrolyte accessibility into the electrodes (increase), as well as the temperature changes during the long-tern cycling tests. It is believed that the cycling stability of the MXene-based MSCs can be further improved by conducting the electrochemical tests in a completely oxygen-free, isothermal environment.

In order to demonstrate its flexible nature, the interdigital L-s-$Ti_3C_2T_x$ MSC on glass substrate was glued to a scotch tape followed by careful peeling off. This led to transfer of the entire architecture onto the scotch tape substrate. As shown in Fig. 5a, the transferred MXene device shows good flexibility with no obvious cracks after repeated bending for 100 times with a bending angle of 60°. After coating with a PVA/H_2SO_4 gel electrolyte, the electrochemical performance of the flexible L-s-$Ti_3C_2T_x$ MSC was tested by recording CVs and charge-discharge profiles (Fig. 5b and c). This flexible device exhibited comparable areal capacitances to its original rigid architecture on glass substrate before transfer, with only 7-12% lower values (Fig. 5d). This is a good demonstration that MXene-based MSCs can be easily transferred and made into flexible devices.

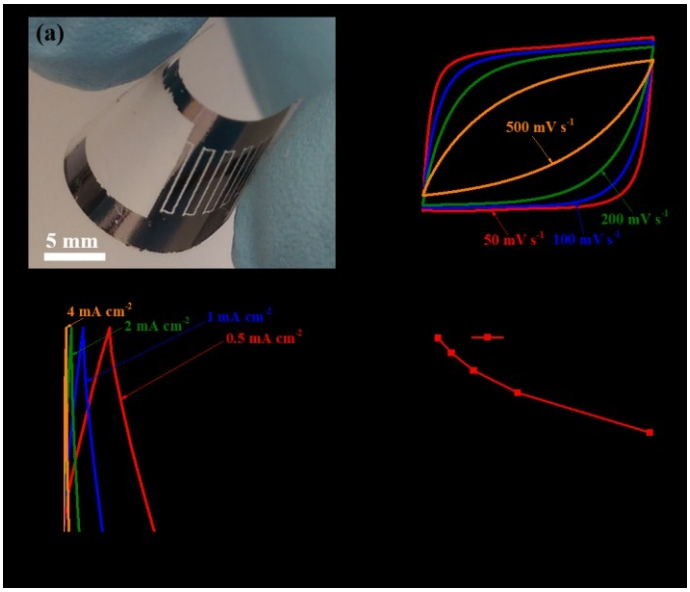

Fig. 5 (a) Digital photograph showing the transferred L-s-$Ti_3C_2T_x$ MXene MSC on to a flexible scotch tape, and the corresponding (b) CVs, (c) charge-discharge curves, and (d) variation in areal capacitances with scan rates.

The volumetric energy and power densities of the all-MXene (L-s-$Ti_3C_2T_x$) MSCs were compared with the state-of-the-art performance metrics, as shown in Fig. 6. The all-MXene MSC exhibited energy density values in the range of 11-18 mWh cm^{-3} with corresponding power densities in the range of 0.7-15 W cm^{-3}. These values are comparable to those of Li-based thin-film batteries (10 mWh cm^{-3}),[8, 10] and superior to those of MSCs based on other classes of materials including carbon (E = 0.15-9 mWh cm^{-3}),[7-10, 13, 16-18, 25, 57] metal oxides (1-5 mWh cm^{-3}) [20, 21, 25,

View Article Online
DOI: 10.1039/C6EE01717G

[59] and conducting polymers (5-11 mWh cm^{-3}) [60, 61] fabricated by various techniques. The outstanding performance of the all-MXene MSCs originates from the electrochemical characteristics of $Ti_3C_2T_x$, including its high electrical conductivity, rapid intercalation between the sheets, fast pseudocapacitive contribution, and hydrophilic surface of MXene helping electrolyte infiltration.[29] Further improvement in MSC performance can be reached upon optimization of MXene flake size, thickness, composition, and the architecture of MXene-based MSC devices.

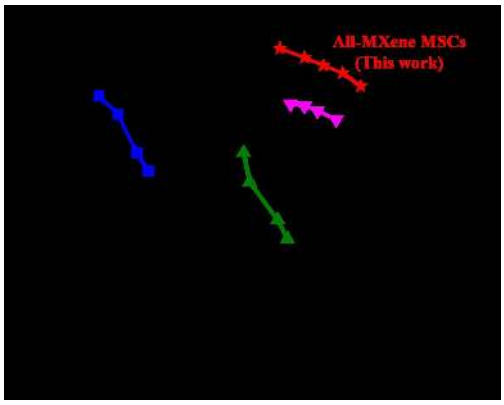

Fig. 6 (a) Ragone plot displaying the volumetric energy and power densities achieved by the all-MXene MSCs in this work with comparison to that of Li thin-film batteries[8, 10], and carbon[7-10, 13, 16-18, 25, 57], metal oxide[20, 21, 25, 59], or conducting polymer-based[60, 61] MSCs.

Conclusions

We have demonstrated the fabrication of novel, noble-metal-free, solid-state all-$Ti_3C_2T_x$ MXene MSC devices. The large-flake L-$Ti_3C_2T_x$ layer was used as the current collector and small-flake s-$Ti_3C_2T_x$ as the active material. The devices exhibited high capacitances and excellent rate-capability. A high areal capacitance of 27.3 mF cm^{-2} at 20 mV s^{-1} and a volumetric capacitance of 356.8 F cm^{-3} at 0.2 mA cm^{-2} were achieved. The L-s-$Ti_3C_2T_x$ MSC also displayed good cycling stability of over 100% capacitance retention after 10,000 cycles at a scan rate of 50 mV s^{-1} after removing oxygen in the electrolyte. The L-s-$Ti_3C_2T_x$ MSC manufactured on a glass substrate can be easily transferred to a flexible substrate while preserving its excellent electrochemical performance. This study opens up a plethora of possible designs of on-chip devices employing a large family of MXenes and their heterostructures.

Experimental

Preparation of L-$Ti_3C_2T_x$

Synthesis of Ti_3AlC_2 MAX phase has been described in previous studies.[39] $Ti_3C_2T_x$ MXene powder was prepared by the following etching procedures: 1 g of Ti_3AlC_2 powder was slowly added into a mixture solution of 1 g lithium fluoride (LiF, Alfa Aesar, 98+ %) in 20 ml 6 M hydrochloric acid (HCl, Fisher, technical grade, 35-38%), and followed by stirring at 35 °C for 24 h. The acidic suspension was washed with 100 ml of deionized (DI) water and centrifuged until pH ≥ 6 is reached and stable dark green supernatant of L-$Ti_3C_2T_x$ was collected after 30 min centrifugation at 3500 rpm. The concentration of L-$Ti_3C_2T_x$ solution was measured by filtering specific amounts of colloidal solution through a polypropylene filter (3501 Coated PP, Celgard LLC, Charlotte, NC), followed by drying at room temperature for two days under vacuum.

Preparation of s-$Ti_3C_2T_x$

The s-$Ti_3C_2T_x$ was simply prepared by further sonicating L-$Ti_3C_2T_x$ colloidal solution using probe sonication (power: 250 W, and 50% amplitude) in a cold bath (-10 °C) for 30 min followed by centrifugation at 3500 rpm for another 30 min. The supernatant was collected as the s-$Ti_3C_2T_x$ colloidal solution.

Fabrication of on-chip MXene micro-supercapacitors

Glass slides of 1.5 × 2 cm^2 size (Fischer) were cleaned with a soap solution to remove the dirt followed by ultrasonication in acetone, isopropanol and DI water sequentially for 5 min each and then dried by blowing nitrogen (N_2) gas. Furthermore, the organic matter that may be present on the glass slides was removed by treating them in piranha solution for 1 h. The solution was prepared by mixing sulfuric acid (H_2SO_4, Alfa Aesar, American Chemical Society grade, 95-98%) and hydrogen peroxide (H_2O_2, ACS, 29-32% w/w aqueous solution) in a 3:1 volume ratio. DI water was used to wash the glass slides at the final stage followed by drying by blowing N_2 gas.

All-MXene-based MSCs were fabricated by spray-coating of 300 nm L-$Ti_3C_2T_x$ film directly onto a glass slide as the current collector followed by spray-coating of a s-$Ti_3C_2T_x$ layer as the active material on the area 6 mm in width and 1.5 cm in length. An airbrush and a hot air gun were turned on simultaneously in order to dry each coated layer immediately. Interdigital patterns were produced by utilizing direct laser machining using a 10.6 µm CO_2 laser (Epilog Mini/Helix 8000, Epilog Laser, USA) with pulse duration of 14 µs. Laser power and speed were set to 3% and 30%, respectively. Z-distance between laser and the sample was 5.1 cm. AutoCAD technical drawing software was used to design the interdigital patterns. The laser beam size was 100 µm. Laser power was varied from 0.4 to 3.2 W with increments of 0.4 W. The laser system offers the option of controlling the laser scan rates up to 7.6 cm/s. As depicted in the schematic of Fig. 1, laser patterning was employed at optimum conditions determined by a parametric study. All of the laser experiments were performed under ambient conditions.

We also fabricated devices by using Pt as the current collector, instead of L-$Ti_3C_2T_x$. First, an 80-nm Pt metal film was deposited on a glass substrate by sputtering. MXene film with a thickness of 1 µm was sprayed from the s-$Ti_3C_2T_x$ solution on the device area (6 mm of width and 1.5 cm of length) as described above. MXene patterned films were obtained using the above mentioned laser cutting procedure. This film will henceforth be referred to as Pt/s-$Ti_3C_2T_x$.

The polyvinyl alcohol (PVA)/H_2SO_4 gel electrolyte was prepared by continuously stirring 1g H_2SO_4 (1 g) in 10 ml of 10% wt. aqueous PVA gel (polyvinyl alcohol, M_r, 115,000; Scientific

Polymer Products). The latter was made by dissolving 1 g of PVA powder in 10 ml DI water at 90 °C for 3 hours under continuous stirring until obtaining a clear solution, and then allowed to cool down. The gel electrolyte was carefully dropped onto the interdigital pattern area of the films. After vaporizing the excess water overnight, MXene-based solid-state MSCs were obtained.

Structural Characterization

The morphology of MXene sample was characterized by transmission electron microscope (TEM) (JEOL JEM-2100, Japan) using an accelerating voltage of 200 kV. The TEM samples were prepared by dropping several drops of the solutions onto a copper grid and dried in air overnight. The morphology of the MXene sheets was imaged using a scanning electron microscope (SEM) (Zeiss Supra 50VP, Germany). The electrical conductivities of the samples were measured using a four-point probe (ResTest v1, Jandel Engineering Ltd., Bedfordshire, UK) with a probe distance of 1 mm. The X-ray diffraction (XRD) patterns were measured by a powder diffractometer (Rigaku Smart Lab, USA) with Cu K_α radiation at a step size of 0.02° with 0.5 s dwelling time. The thickness of electrodes was measured by an Optical Profilometer (Zygo NewView 6000).

Electrochemical measurements

The symmetrical MXene MSCs were connected to instrument cables by silver adhesive (Fast drying Ag paint, SPI supplies) in two-electrode configuration. All the electrochemical measurements were done using VMP3 potentiostat (Biologic, France). The cyclic voltammetry tests were performed using a scan rate ranging from 20 to 500 mV/s in the potential window of 0 to 0.6 V to avoid material oxidation.[45] The capacitances were calculated by integrating the discharge portion of the CVs. Galvanostatic cycling was carried out using a current density of 0.2, 0.5, 1, 2, and 4 mA cm^{-2} in the same potential window. The capacitances were calculated from the slopes of the discharge curves. The electrochemical impedance spectroscopy was performed at open circuit potential (OCP), with small sinusoidal amplitude of 5 mV, and frequencies of 50 mHz to 10 kHz. Since the weight of the electrode material is almost negligible in MSCs, the areal and volumetric capacitances were used to evaluate the electrochemical performance of microsupercapacitors.[1]

Acknowledgements

This work was supported by the Fluid Interface Reactions, Structures and Transport (FIRST) Center, an Energy Frontier Research Center funded by the U.S. Department of Energy, Office of Science, and Office of Basic Energy Sciences. YP was supported by Ministry of Science and Technology of Taiwan under grants No. 104-2917-I-606-001. The authors wish to thank Professor James Tangorra at Drexel University for their assistance and use of their laser cutter, and Professor Adam Fontecchio for use of their Profilometer. XRD, SEM, and TEM investigations were performed at the Centralized Research Facilities (CRF) at Drexel University.

Notes and References

View Article Online
DOI: 10.1039/C6EE01717G

1. M. Beidaghi and Y. Gogotsi, *Energy Environ. Sci.*, 2014, **7**, 867-884.
2. Z. L. Wang, *Nano Today*, 2010, **5**, 512-514.
3. Z. L. Wang and W. Wu, *Angew. Chem. Int. Ed.*, 2012, **51**, 11700-11721.
4. H. Hu, Z. Pei and C. Ye, *Energy Storage Materials*, 2015, **1**, 82-102.
5. P. Huang, C. Lethien, S. Pinaud, K. Brousse, R. Laloo, V. Turq, M. Respaud, A. Demortière, B. Daffos, P. L. Taberna, B. Chaudret, Y. Gogotsi and P. Simon, *Science*, 2016, **351**, 691-695.
6. G. Xiong, C. Meng, R. G. Reifenberger, P. P. Irazoqui and T. S. Fisher, *Electroanal.*, 2014, **26**, 30-51.
7. J. Chmiola, C. Largeot, P.-L. Taberna, P. Simon and Y. Gogotsi, *Science*, 2010, **328**, 480-483.
8. M. F. El-Kady and R. B. Kaner, *Nat. Commun.*, 2013, **4**, 1475.
9. D. Pech, M. Brunet, P.-L. Taberna, P. Simon, N. Fabre, F. Mesnilgrente, V. Conédéra and H. Durou, *J. Power Sources*, 2010, **195**, 1266-1269.
10. D. Pech, M. Brunet, H. Durou, P. Huang, V. Mochalin, Y. Gogotsi, P.-L. Taberna and P. Simon, *Nat. Nanotechnol.*, 2010, **5**, 651-654.
11. H. Ben, M. Julian, W. Shuang, I. Jung Bin, C. Carlo, P. Dimos, P. G. Costas and M. Roya, *Nanotechnology*, 2014, **25**, 055401.
12. S.-K. Kim, H.-J. Koo, A. Lee and P. V. Braun, *Adv. Mater.*, 2014, **26**, 5108-5112.
13. W. Gao, N. Singh, L. Song, Z. Liu, A. L. M. Reddy, L. Ci, R. Vajtai, Q. Zhang, B. Wei and P. M. Ajayan, *Nat. Nanotechnol.*, 2011, **6**, 496-500.
14. J. Lin, Z. Peng, Y. Liu, F. Ruiz-Zepeda, R. Ye, E. L. G. Samuel, M. J. Yacaman, B. I. Yakobson and J. M. Tour, *Nat. Commun.*, 2014, **5**, 5714.
15. Z. Niu, L. Zhang, L. Liu, B. Zhu, H. Dong and X. Chen, *Adv. Mater.*, 2013, **25**, 4035-4042.
16. Z. S. Wu, K. Parvez, X. Feng and K. Müllen, *Nat. Commun.*, 2013, **4**, 2487.
17. Z.-S. Wu, K. Parvez, X. Feng and K. Mullen, *J. Mater. Chem. A*, 2014, **2**, 8288-8293.
18. M. Beidaghi and C. Wang, *Adv. Funct. Mater.*, 2012, **22**, 4501-4510.
19. B. Song, L. Li, Z. Lin, Z.-K. Wu, K.-s. Moon and C.-P. Wong, *Nano Energy*, 2015, **16**, 470-478.
20. N. Kurra, N. A. Alhebshi and H. N. Alshareef, *Adv. Energy Mater.*, 2015, **5**, 1401303.
21. W. Si, C. Yan, Y. Chen, S. Oswald, L. Han and O. G. Schmidt, *Energy Environ. Sci.*, 2013, **6**, 3218-3223.
22. L. Cao, S. Yang, W. Gao, Z. Liu, Y. Gong, L. Ma, G. Shi, S. Lei, Y. Zhang, S. Zhang, R. Vajtai and P. M. Ajayan, *Small*, 2013, **9**, 2905-2910.
23. N. Kurra, C. Xia, M. N. Hedhili and H. N. Alshareef, *Chem. Commun.*, 2015, **51**, 10494-10497.
24. J. Feng, X. Sun, C. Wu, L. Peng, C. Lin, S. Hu, J. Yang and Y. Xie, *J. Am. Chem. Soc.*, 2011, **133**, 17832-17838.
25. N. Kurra, Q. Jiang and H. N. Alshareef, *Nano Energy*, 2015, **16**, 1-9.
26. C. Meng, J. Maeng, S. W. M. John and P. P. Irazoqui, *Adv. Energy Mater.*, 2014, **4**, 1301269.
27. M. Acerce, D. Voiry and M. Chhowalla, *Nat. Nanotechnol.*, 2015, **10**, 313-318.

28. O. Mashtalir, M. Naguib, V. N. Mochalin, Y. Dall'Agnese, M. Heon, M. W. Barsoum and Y. Gogotsi, *Nat. Commun.*, 2013, **4**, 1716.
29. M. Naguib, V. N. Mochalin, M. W. Barsoum and Y. Gogotsi, *Adv. Mater.*, 2014, **26**, 992-1005.
30. Y. Xie, M. Naguib, V. N. Mochalin, M. W. Barsoum, Y. Gogotsi, X. Yu, K.-W. Nam, X.-Q. Yang, A. I. Kolesnikov and P. R. C. Kent, *J. Am. Chem. Soc.*, 2014, **136**, 6385-6394.
31. B. Anasori, Y. Xie, M. Beidaghi, J. Lu, B. C. Hosler, L. Hultman, P. R. C. Kent, Y. Gogotsi and M. W. Barsoum, *ACS Nano*, 2015, **9**, 9507-9516.
32. M. Naguib, M. Kurtoglu, V. Presser, J. Lu, J. Niu, M. Heon, L. Hultman, Y. Gogotsi and M. W. Barsoum, *Adv. Mater.*, 2011, **23**, 4248-4253.
33. M. Naguib, O. Mashtalir, J. Carle, V. Presser, J. Lu, L. Hultman, Y. Gogotsi and M. W. Barsoum, *ACS Nano*, 2012, **6**, 1322-1331.
34. C. E. Ren, K. B. Hatzell, M. Alhabeb, Z. Ling, K. A. Mahmoud and Y. Gogotsi, *J. Phys. Chem. Lett.*, 2015, **6**, 4026-4031.
35. Y. Dall'Agnese, P. Rozier, P.-L. Taberna, Y. Gogotsi and P. Simon, *J. Power Sources*, 2016, **306**, 510-515.
36. M. Ghidiu, M. R. Lukatskaya, M.-Q. Zhao, Y. Gogotsi and M. W. Barsoum, *Nature*, 2014, **516**, 78-81.
37. X. Ji, K. Xu, C. Chen, B. Zhang, Y. Ruan, J. Liu, L. Miao and J. Jiang, *Phys. Chem. Chem. Phys.*, 2016, **18**, 4460-4467.
38. Z. Ling, C. E. Ren, M.-Q. Zhao, J. Yang, J. M. Giammarco, J. Qiu, M. W. Barsoum and Y. Gogotsi, *Proc. Natl. Acad. Sci. U. S. A.*, 2014, **111**, 16676-16681.
39. M.-Q. Zhao, C. E. Ren, Z. Ling, M. R. Lukatskaya, C. Zhang, K. L. Van Aken, M. W. Barsoum and Y. Gogotsi, *Adv. Mater.*, 2015, **27**, 339-345.
40. Y. Dall'Agnese, P.-L. Taberna, Y. Gogotsi and P. Simon, *J. Phys. Chem. Lett.*, 2015, **6**, 2305-2309.
41. X. Wang, S. Kajiyama, H. Iinuma, E. Hosono, S. Oro, I. Moriguchi, M. Okubo and A. Yamada, *Nat. Commun.*, 2015, **6**, 6544.
42. S. J. Kim, M. Naguib, M. Zhao, C. Zhang, H.-T. Jung, M. W. Barsoum and Y. Gogotsi, *Electrochim. Acta*, 2015, **163**, 246-251.
43. O. Mashtalir, M. R. Lukatskaya, M.-Q. Zhao, M. W. Barsoum and Y. Gogotsi, *Adv. Mater.*, 2015, **27**, 3501-3506.
44. X. Liang, A. Garsuch and L. F. Nazar, *Angew. Chem. Int. Ed.*, 2015, **54**, 3907-3911.
45. M. R. Lukatskaya, O. Mashtalir, C. E. Ren, Y. Dall'Agnese, P. Rozier, P. L. Taberna, M. Naguib, P. Simon, M. W. Barsoum and Y. Gogotsi, *Science*, 2013, **341**, 1502-1505.
46. M. Ghaffari, Y. Zhou, H. Xu, M. Lin, T. Y. Kim, R. S. Ruoff and Q. M. Zhang, *Adv. Mater.*, 2013, **25**, 4879-4885.
47. N. Jung, S. Kwon, D. Lee, D.-M. Yoon, Y. M. Park, A. Benayad, J.-Y. Choi and J. S. Park, *Adv. Mater.*, 2013, **25**, 6854-6858.
48. J. Yan, Q. Wang, T. Wei, L. Jiang, M. Zhang, X. Jing and Z. Fan, *ACS Nano*, 2014, **8**, 4720-4729.
49. A. D. Dillon, M. J. Ghidiu, A. L. Krick, J. Griggs, S. J. May, Y. Gogotsi, M. W. Barsoum and A. T. Fafarman, *Adv. Funct. Mater.*, 2016, **26**, 4162-4168.
50. B. Mendoza-Sánchez and Y. Gogotsi, *Adv. Mater.*, 2016, in press.
51. M. Ghidiu, M. Naguib, C. Shi, O. Mashtalir, L. M. Pan, B. Zhang, J. Yang, Y. Gogotsi, S. J. L. Billinge and M. W. Barsoum, *Chem. Commun.*, 2014, **50**, 9517-9520.
52. J. Halim, S. Kota, M. R. Lukatskaya, M. Naguib, M.-Q. Zhao, E. J. Moon, J. Pitock, J. Nanda, S. J. May, Y. Gogotsi and M. W. Barsoum, *Adv. Funct. Mater.*, 2016, **26**, 3118-3127.
53. M. Naguib, J. Halim, J. Lu, K. M. Cook, L. Hultman, Y. Gogotsi and M. W. Barsoum, *J. Am. Chem. Soc.*, 2013, **135**, 15966-15969.
54. H. Ghassemi, W. Harlow, O. Mashtalir, M. Beidaghi, M. R. Lukatskaya, Y. Gogotsi and M. L. Taheri, *J. Mater. Chem. A*, 2014, **2**, 14339-14343.
55. C. E. Ren, M.-Q. Zhao, T. Makaryan, J. Halim, M. Boota, S. Kota, B. Anasori, M. W. Barsoum and Y. Gogotsi, *ChemElectroChem*, 2016, **3**, 689-693.
56. Z. Liu, Z.-S. Wu, S. Yang, R. Dong, X. Feng and K. Müllen, *Adv. Mater.*, 2016, **28**, 2217-2222.
57. J. Lin, C. Zhang, Z. Yan, Y. Zhu, Z. Peng, R. H. Hauge, D. Natelson and J. M. Tour, *Nano Lett.*, 2013, **13**, 72-78.
58. R. R. Devarapalli, S. Szunerits, Y. Coffinier, M. V. Shelke and R. Boukherroub, *ACS Appl. Mater. Interfaces*, 2016, **8**, 4298-4302.
59. T. M. Dinh, K. Armstrong, D. Guay and D. Pech, *J. Mater. Chem. A*, 2014, **2**, 7170-7174.
60. Q. Jiang, N. Kurra and H. N. Alshareef, *Adv. Funct. Mater.*, 2015, **25**, 4976-4984.
61. K. Wang, H. Wu, Y. Meng and Z. Wei, *Small*, 2014, **10**, 14-31.